Ab initio and atomistic study of generalized stacking fault energies in Mg and Mg–Y alloys

Z Pei[1,2]**, L-F Zhu**[1]**, M Friák**[1,2,5]**, S Sandlöbes**[1]**, J von Pezold**[1]**,
H W Sheng**[3]**, C P Race**[1]**, S Zaefferer**[1]**, B Svendsen**[1,2,4]**, D Raabe**[1]
and J Neugebauer[1]

[1] Max-Planck-Institut für Eisenforschung GmbH, Max-Planck-Strasse 1,
D-40237 Düsseldorf, Germany
[2] Aachen Institute for Advanced Study in Computational Engineering Science
(AICES), RWTH Aachen University, Schinkelstraße 2, D-52062 Aachen,
Germany
[3] School of Physics, Astronomy and Computational Sciences,
George Mason University, Fairfax, VA 22030, USA
[4] Material Mechanics, Faculty of Georesources and Materials Engineering,
RWTH Aachen University, Schinkelstraße 2, D-52062 Aachen, Germany
E-mail: m.friak@mpie.de

Abstract. Magnesium–yttrium alloys show significantly improved room
temperature ductility when compared with pure Mg. We study this interesting
phenomenon theoretically at the atomic scale employing quantum-mechanical
(so-called *ab initio*) and atomistic modeling methods. Specifically, we have
calculated generalized stacking fault energies for five slip systems in both
elemental magnesium (Mg) and Mg–Y alloys using (i) density functional theory
and (ii) a set of embedded-atom-method (EAM) potentials. These calculations
predict that the addition of yttrium results in a reduction in the unstable stacking
fault energy of basal slip systems. Specifically in the case of an I_2 stacking
fault, the predicted reduction of the stacking fault energy due to Y atoms was
verified by experimental measurements. We find a similar reduction for the stable
stacking fault energy of the $\{11\bar{2}2\}\langle11\bar{2}3\rangle$ non-basal slip system. On the other

[5] Author to whom any correspondence should be addressed.

IOP Institute of Physics Φ DEUTSCHE PHYSIKALISCHE GESELLSCHAFT

hand, other energies along this particular γ-surface profile increase with the addition of Y. In parallel to our quantum-mechanical calculations, we have also developed a new EAM Mg–Y potential and thoroughly tested its performance. The comparison of quantum-mechanical and atomistic results indicates that the new potential is suitable for future large-scale atomistic simulations.

Contents

1. Introduction

Magnesium alloys are promising candidate materials for lightweight industrial applications [1, 2]. Unfortunately, a wider use of magnesium and many Mg-based alloys is impeded by their poor room-temperature ductility, which is caused by basal-type texturing and limited available deformation mechanisms. It is known [3] that addition of Y and/or rare-earth elements increases the ductility by texture weakening and higher activity of non-basal slip systems. Specifically, shear deformations with a component along the $\langle 0001 \rangle$ axis, including twinning and $\langle c+a \rangle$ slip systems, were shown (e.g. in [4]) to determine the mechanical behavior of hcp metals (figure 1). The limitation to mainly basal $\langle a \rangle$ slip and tensile twinning in pure Mg and most commercial wrought Mg alloys causes strain localization in a few shear bands and early fracture of the materials along these shear bands. It has been shown experimentally [5] that alloying Y leads to higher activation of non-basal deformation modes, i.e. non-basal dislocation slip and compression twinning, and consequently to much enhanced ductility at room temperature. Nucleation and mobility energies of dislocations, both perfect and dissociated dislocations, are related to the stable and unstable stacking fault energies which are available via atomistic calculations.

Different slip mechanisms in Mg have been intensively studied both experimentally [5–8] and theoretically [4, 9–11]. Theoretical studies generally focused on calculating so-called generalized stacking fault energy (GSFE) profiles obtained by sliding one half of a crystal over the second half across a given glide plane. As shown by Vitek [12], these energy profiles are closely connected with the motion of dislocations and the plasticity of materials in general. GSFEs of important planes along different slip directions were calculated employing both density functional theory (DFT) and the embedded atom method (EAM) for pure Mg [13–17].
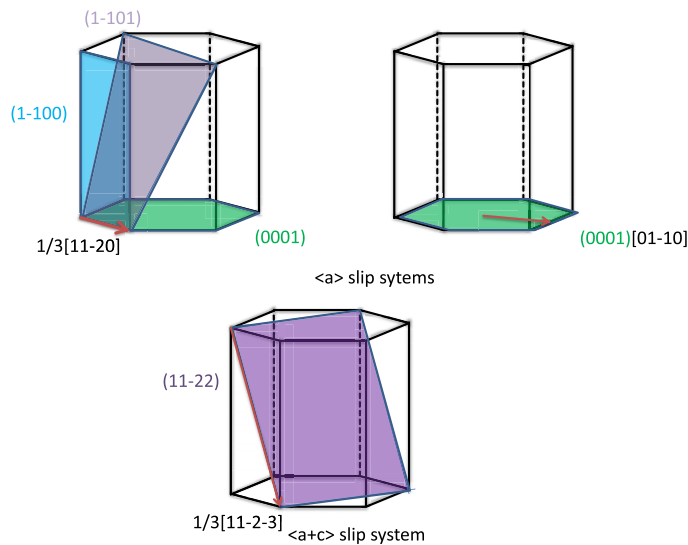
Figure 1. Schematic drawing showing possible slip systems in hcp metals. Specifically the (0001)[01–10] is considered here for studying the I_2 stacking fault.

It was shown, for example, that maxima occurring along GSFE profiles, so-called unstable stacking fault energies (USFEs), determine the behavior of slip modes and thus the ductility in fcc metals [18].

Our study is motivated by the fact that rather little is known about GSFEs in Mg–Y alloys, especially in the case of non-basal deformation modes (see e.g. table 1). Therefore, we study and compare the influence of Y additions on the behavior of both basal and non-basal slip systems. Our aim was to provide results that will contribute to the understanding of enhanced room temperature ductility of Mg–Y alloys [5] and to the design of ductile Mg-based materials in the future.

Due to the fact that it is experimentally very difficult to obtain a deeper insight into various mechanisms that are simultaneously active in Mg alloys at atomic scale, we employ theoretical methods as these allow for decomposing this complexity into individual processes and studying them separately. Unfortunately, even theoretical modeling is limited by available computer resources, especially in the case of state-of-the-art quantum-mechanical calculations. The predictive power and reliability of these calculations can nowadays be applied only to problems involving a few hundreds of atoms. As processes related to the plasticity of materials typically span over much larger scales, methods based on inter-atomic potentials are often used instead. For these simulations, well-tested and reliable potentials are necessary. Therefore, we have not only employed quantum-mechanical calculations but, in a complementary manner, we have also developed a new Mg–Y EAM potential. We first carefully validated our potential and only after this then used it to simulate processes involving so many atoms that quantum-mechanical calculations would be prohibitively long. In order to verify our theoretical predictions, an experimental TEM analysis of the I_2 stacking fault was performed and confirmed our theoretical findings.

Table 1. Independent deformation modes in hcp crystals.

Slip systems	Direction	Plane	Independent deformation modes
$\{0001\}\langle 11\bar{2}0\rangle$	$\langle a\rangle$	Basal	2
$\{10\bar{1}0\}\langle 11\bar{2}0\rangle$	$\langle a\rangle$	Prismatic	2
$\{10\bar{1}l\}\langle 11\bar{2}0\rangle$	$\langle a\rangle$	Pyramidal	4
$\{hki0\}\langle 0001\rangle$	$\langle c\rangle$	Prismatic	–
$\{hkil\}\langle 11\bar{2}3\rangle$	$\langle a+c\rangle$	Pyramidal	5

Table 2. Different stoichiometries with corresponding supercell sizes and slip systems in EAM calculations.

Slip systems	Supercell size	No. of atoms
$\{0001\}\langle 11\bar{2}0\rangle$	$2 \times 2 \times 6$	48
$\{10\bar{1}0\}\langle 11\bar{2}0\rangle$	$2 \times 2 \times 7$	56
$\{0001\}\langle 10\bar{1}0\rangle$	$4 \times 4 \times 6$	192
$\{10\bar{1}1\}\langle 11\bar{2}0\rangle$	$4 \times 4 \times 3$	192
$\{11\bar{2}2\}\langle 11\bar{2}3\rangle$	$12 \times 6 \times 2$	1728

2. Methodology

2.1. γ-surface simulations

Employing theoretical methods, slip deformation modes can be studied by calculating generalized stacking fault energies, known as γ-surfaces [12]. Key properties of slip deformation modes such as the Peierls barrier as well as stacking fault energies can be deduced from the γ-surfaces. We determine the generalized stacking fault energies by incrementally shifting the upper half crystal along the slip direction and calculating the total energy of the system as a function of the applied shift vector. In order to facilitate the consideration of a single stacking fault, and so allow us to reduce the required system dimensions, we added the applied shift vector to the lattice vector along the glide plane normal (in our case the glide plane normal is denoted as the z-direction). For the minimization after each incremental shift, atomic positions are constrained along the lateral dimensions of the glide plane, but atoms can reduce the total energy of the system by relaxing in the direction perpendicular to the studied glide plane.

In order to eliminate any spurious interactions between the interface (i.e. the glide plane) and its periodic images, the supercell size must be sufficiently large. We therefore converged the GSFE with respect to the number of atomic planes parallel to the fault plane. For example, in order to determine an optimum number of atomic planes for the $\{0001\}\langle 11\bar{2}0\rangle$ slip system, supercells with 2, 4, 6, 8 and 12 layers along the $\langle 11\bar{2}0\rangle$ direction, the z-direction (parallel to the plane normal), were used to calculate GSFEs. The GSFE difference between 6-layer ($2 \times 2 \times 6$, 24 atoms) and 12-layer ($2 \times 2 \times 12$, 48 atoms) supercells is less than 1%. Therefore, supercells with more than six layers are considered large enough. In our case, a 48-atom supercell was employed to obtain a realistically low Y concentration. Converged supercell sizes of all the other slip systems considered were determined similarly (see table 2). In calculations of Mg–Y alloys, one Mg atom is replaced by a Y atom on the first plane (with the smallest value of the

Table 3. DFT-computed lattice parameters for pure Mg and Mg–Y alloys with different stoichiometries with corresponding supercell sizes and slip systems.

Stoichiometry	a (Å)	c/a	Supercell size	Atom no.	Slip systems
Mg	3.1886	1.6261	$2 \times 2 \times 2$	16	All slip systems
$Mg_{55}Y$	3.2004	1.6253	$2 \times 2 \times 14$	56	$\{10\bar{1}0\}\langle11\bar{2}0\rangle$
$Mg_{47}Y$	3.2064	1.6215	$2 \times 2 \times 12$	48	$\{0001\}\langle11\bar{2}0\rangle$, $\{0001\}\langle10\bar{1}0\rangle$, $\{10\bar{1}1\}\langle11\bar{2}0\rangle$, $\{11\bar{2}2\}\langle11\bar{2}3\rangle$

z-axis in the coordinate system). Therefore, in $Mg_{55}Y$ the concentration of Y is 1.82 at.% and 2.08 at.% for $Mg_{47}Y$ in all the other considered slip systems.

In the case of the γ-surface for the $\{11\bar{2}2\}$ plane, two perpendicular vectors ($\frac{1}{3}[11\bar{2}3]$ and $[10\bar{1}0]$) are selected on the plane. All displacements in the slip plane can be obtained by a combination of these two vectors. Suppose x and y are fractional displacements along the two directions; the GSF vector $\vec{f}$ may be written as $\vec{f} = x\frac{1}{3}[11\bar{2}3] + y\,[10\bar{1}0]$, where $0 \leqslant x \leqslant 1$ and $0 \leqslant y \leqslant 1$. More details about the calculation of the γ-surface can be found in [19].

2.2. Parameters of ab initio calculations

In our work, we calculate GSFE profiles using both DFT [20, 21] and the EAM [22] (using the LAMMPS [23] package.). Our DFT calculations were carried out using the projector augmented wave method [39] and the electronic exchange–correlation effects were described by the generalized gradient approximation [40] as implemented in the Vienna *Ab initio* Simulation Package (VASP) [41, 42]. A plane wave energy cut-off of 350 eV is used for both pure Mg and the Mg–Y alloys. The Brillouin zone was sampled using dense Monkhorst–Pack [43] k-point meshes that were chosen to ensure a convergence of the total energy to within 1 meV per atom. Atomic relaxations were performed until the energy and forces converged to 10^{-7} eV and 10^{-3} eV Å^{-1}, respectively. To test our computational parameters, we have calculated the lattice parameters of pure Mg. The results, $a = 3.1886$ Å and $c/a = 1.6261$ (table 3), are in good agreement with experimental data suggesting $a = 3.21$ Å and $c/a = 1.624$ [44].

2.3. Development of Mg–Y embedded atom method potential

Empirical potentials provide a means of exploring the physics of systems of atoms on length- and time-scales currently inaccessible to more computationally expensive *ab initio* techniques. Such potentials seek to approximate the energy of a system of atoms, and the forces between those atoms, as a classical function of the relative positions of the atoms treated as point particles. The key attributes of such potentials are: (i) the level of physics they aim to capture, i.e. whether they are simple pair potentials or attempt to capture many-atom effects and whether they are functions only of atomic separations or also of bond angles; (ii) the nature of the functions used in the fitted potential, which is to say, the extent to which those functions have a (perhaps physically motivated) prescribed form versus being, say, piecewise spline fitted; and (iii) the data to which those functions are fitted, which may be energies and elastic properties from experiment and *ab initio* calculations or individual atomic forces from *ab initio* calculations for a set of atomic configurations. The key issue for empirical potentials, especially

when they are to be used to explore systems beyond the reach of *ab initio*, is their *transferability*: it is one thing to correctly reproduce the properties to which a potential is fitted and quite another to provide accurate predictions of 'unseen' data. As no existing potential (e.g. [45]) has been developed specifically for GSFE calculations, we provide a new one.

In this study, an EAM interatomic potential was developed to describe the Mg–Y system, which has the following formalism [22, 24]: $E_{\text{tot}} = \Sigma_{i,j} \phi(r_{ij}) + \Sigma_i F(n_i)$, where $n = \Sigma_j \rho(r_{ij})$ and $\phi(r)$, $\rho(r)$ and $F(n_i)$ are the pair, density and embedding functions. In this work, the three functions $\phi(r)$, $\rho(r)$ and $F(n_i)$ are represented with quintic spine interpolations [25]. We used 15 equidistant spline knots for both the pair and the density functions (in the fitting range of 0.5–6.5 Å), and 6 spline knots for the embedding function. For the Mg–Y binary system, a total number of 83 parameters was fitted.

The EAM potential was developed based on the force-matching method [25, 26] as implemented in the POTFIT package [27]. To this end, a first-principles database was first established to provide a coarse-grained potential energy surface (PES) of the Mg–Y system. The database was constructed to encompass a wide range of atomic configurations, including all crystalline phases in this alloy system, as well as their derivative structures such as defects, crystal equations of state, deformation paths, melting and cooling trajectories, etc. In addition to six crystal structures of Mg and Y (i.e. hcp, bcc, fcc, 9R, diamond and sc structures), three crystallographic types of Mg–Y intermetallic compounds [28] are considered in this work, including $Mg_{24}Y_5$ ($I\bar{4}3m$), Mg_2Y ($P6_3/mmc$) and MgY ($Pm3m$).

Ab initio molecular dynamics (MD) simulation [29] was conducted to obtain liquid structures as well as their trajectories along the heating and cooling processes. Altogether, around 700 configurations (with each configuration typically containing 100 atoms) were selected and subjected to DFT calculations using the pseudopotential and plane-wave method implemented in the VASP [41, 42]. The derived PES (the potential energy and stress tensors of each configuration, forces on each atom and elastic constants of two reference structures) was further modified to match the experimental values of the lattice parameter and cohesive energy of Mg and Y, and was then utilized to parameterize the EAM potential for the Mg–Y system. A similar practice can be found in [25]. During potential fitting, *ad hoc* EAM potentials were employed in classical MD to probe deeper potential basins on the PES, with new configurations added to the previously built potential database for a new round of EAM parameterization. Several iterations were performed until self-consistency between *ab initio* and EAM calculations was reached.

To demonstrate the overall performance of the as-developed EAM potential, we compare the present EAM model with previous models for Mg and Y in terms of the accuracy of predicting a set of material properties, as shown in tables 4 and 5. The performance of the EAM potential for Mg–Y alloys can be seen from figure 2, where the equations of state of the crystalline phases derived from the EAM model and the *ab initio* treatment are provided. The cohesive energies of the intermetallic compounds, with tabulated lattice parameters, are listed in table 6 for comparison. The general agreement between EAM and *ab initio* calculations is satisfactory. The as-developed EAM potential is available from https://sites.google.com/site/eampotentials/Home/MgY.

3. Results and discussion

Our quantum-mechanical and atomistic calculations of GSFE profiles include five slip systems for both pure Mg and Mg–Y. Specifically, we consider the three $\langle a \rangle$-type slip systems

Table 4. Physical properties of Mg predicted by the present EAM model and other EAM models. E_c is the cohesive energy, E_ν^f is the relaxed vacancy formation energy, E_ν^m is the migration energy of the vacancy.

	Experiment/theory	Present model	Sun[a]	Liu[b]
a (Å)	3.21[c]	3.21 (300 K)	3.206	3.206
c/a ratio	1.623[c]	1.610	1.623	1.623
E_c (eV atom^{-1})	1.510[d]	1.510	1.516	1.516
C_{11} (GPa)	59.5[e]	59.5	69.6	61.8
C_{12} (GPa)	26.1[e]	25.7	25.3	25.9
C_{13} (GPa)	21.8[e]	20.9	16	21.9
C_{33} (GPa)	61.6[e]	62.7	69.5	67.5
C_{44} (GPa)	16.4[e]	15.8	12.8	18.2
E_ν^f (eV)	$0.59 \approx 0.89$[b]	0.62	0.88	0.87
E_ν^m (eV)	0.39[b]	0.47	0.64	
$E_{surface}$ (mJ m^{-2})	680[f]	480[g]		495
$E_{fcc-hcp}$ (eV)	0.011[b], 0.007[h]	0.006	0.012	0.015
$E_{bcc-hcp}$ (eV)	0.028[b]	0.024	0.014	0.018
T_m (K) (hcp)	923[i]	850		

[a] Sun *et al* [30].
[b] Liu *et al* [31].
[c] Barrett and Massalski [34].
[d] Kittel [35].
[e] Simons and Wang [36].
[f] de Boer [37]
[g] Average of basal plane and prism plane surface energies.
[h] First-principles results as a part of this work.
[i] Campbell [38].

($\{0001\}\langle11\bar{2}0\rangle$, $\{10\bar{1}0\}\langle11\bar{2}0\rangle$ and $\{10\bar{1}1\}\langle11\bar{2}0\rangle$), and the second pyramidal slip system ($\{11\bar{2}2\}$ $\langle11\bar{2}3\rangle$), which contributes to shear deformation out of the basal plane, as well as the $\{0001\}\langle10\bar{1}0\rangle$ slip system, which is related to the intrinsic stacking fault I$_2$ (I$_2$ SF). The I$_2$ stacking fault is formed when the [0001]-vector is altered by addition of $\frac{1}{3}\langle10\bar{1}0\rangle$. If we assign letters A, B and C to three possible stacking configurations of (0001) planes (in analogy to the stacking order of (111) planes in face-centered cubic lattices), the normal alternating hcp-stacking (. . . ABABABAB . . .) is locally changed to an (. . . ABABCACA . . .) stacking. Thus the influence of Y on the energetics of the I$_2$ stacking fault can be studied by GSFE calculations. This part of our study represents a continuation of our previous experimental and theoretical study on the intrinsic stacking fault, I$_1$ (see [46] for details).

3.1. Basal-plane generalized stacking fault calculations

3.1.1. Basal-plane slip systems. The computed GSFEs of $\{0001\}$ along $\langle11\bar{2}0\rangle$ are plotted as a function of the shift vector for pure Mg and the Mg–Y alloy in figure 3. The USFEs based on DFT calculations for pure Mg and the Mg–Y alloy (Mg$_{47}$Y, 2.08 at.% Y) are 0.276 and 0.214 J m^{-2}, respectively. The USFEs are thus predicted to be reduced by 22.5% due to the

Table 5. Physical properties of Y predicted by the present EAM model and other EAM models. E_c is the cohesive energy, E_ν^f is the relaxed vacancy formation energy, E_ν^m is the migration energy of the vacancy.

	Experiment/theory	Present model	Hu[a]	Baskes[b]
a (Å)	3.65[c]	3.65 (300 K)	3.65	3.65
c/a ratio	1.57[c]	1.57	1.57	1.57
E_c (eV atom^{-1})	4.37[d]	4.37	4.37	
C_{11} (GPa)	77.9[e]	78.3		
C_{12} (GPa)	28.5[e]	26.8		
C_{13} (GPa)	21.0[e]	21.9		
C_{33} (GPa)	76.9[e]	77.2		
C_{44} (GPa)	24.3[e]	21.7		
E_ν^f (eV)	1.50[f]	1.70	1.22	1.25
E_ν^m (eV)		0.66	0.59	
$E_{surface}$ (mJ m^{-2})	1125[g]	830	868	625
$E_{fcc-hcp}$ (eV)		−0.03		
$E_{bcc-hcp}$ (eV)	0.022[g]	0.020		
T_m (K) (hcp)	1796[h]	1810		

[a] Hu *et al* [32].
[b] Baskes and Johnson [33].
[c] Barrett and Massalski [34].
[d] Kittel [35].
[e] Simons and Wang [36].
[f] Boer *et al* [37].
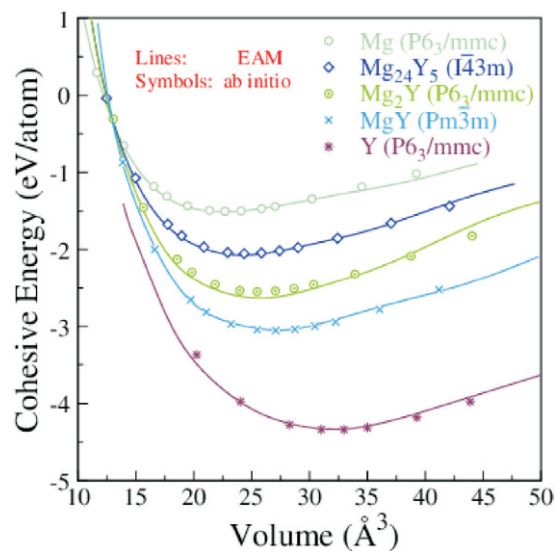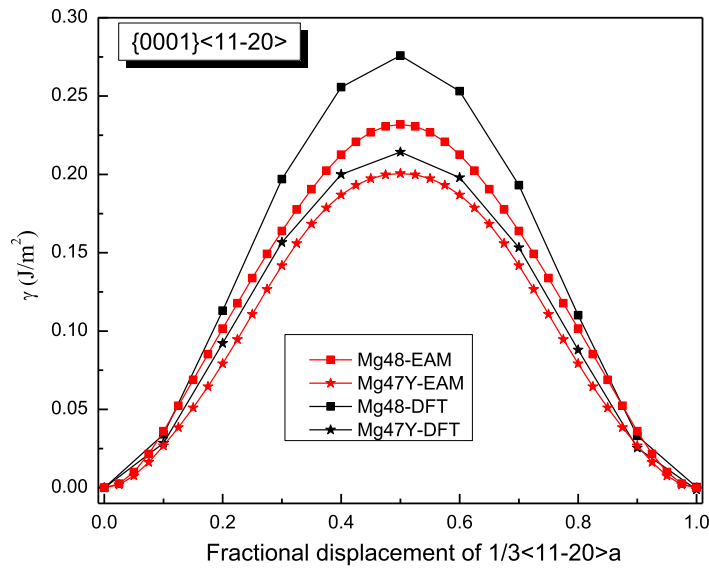[g] First-principles results as a part of this work.
[h] Campbell [38].

Figure 2. Comparison of *ab initio* and EAM calculations of the cohesive energies of Mg–Y alloys at different volumes.

Table 6. Cohesive energies of Mg–Y intermetallic compounds predicted by EAM and *ab initio* calculations. The lattice parameters are taken from [28].

Compound	Lattice parameter	Cohesive energy *ab initio* (eV atom^{-1})	Cohesive energy EAM (eV atom^{-1})
MgY ($Pm3m$)	$a = 3.790$ Å	3.06	3.05
Mg$_2$Y ($P6_3/mmc$)	$a = 6.037$ Å	2.55	2.64
	$c = 752$ Å		
Mg$_{24}$Y$_5$ ($I\bar{4}3m$)	$a = 3.790$ Å	2.05	2.07

Figure 3. GSFE profiles calculated for Mg and Mg–Y alloys as a function of crystal displacement along the $\langle 11\bar{2}0 \rangle$ direction in the basal plane. The total displacement (corresponding to 1.0 at the horizontal axis in the figure) is the respective lattice parameter a of either elemental Mg or the Mg$_{47}$Y alloy. The unstable stacking fault corresponds to the displacement of $0.5a$.

addition of Y. This finding is in agreement with previous DFT results [13] (0.288 J m^{-2} in Mg is reduced to 0.248 J m^{-2} in Mg–Y alloys). When studying the same GSFE employing atomistic EAM potentials, the trend is qualitatively the same but the reduction (from 0.233 J m^{-2} in Mg to 0.190 J m^{-2} in Mg$_{47}$Y) is slightly smaller, 18.5%. The GSFE curves obtained by DFT and EAM calculations are similar with variations in the USFE ranging between 12% and 15% for Mg and the Mg–Y alloy. We can therefore conclude that both methods consistently predict the GSFE barriers to be reduced upon Y additions.

3.1.2. Prismatic $\{10\bar{1}0\}\langle 11\bar{2}0 \rangle$ slip system. The GSFE curves of the prismatic $\langle a \rangle$ slip system $\{10\bar{1}0\}\langle 11\bar{2}0 \rangle$ for pure Mg and the Mg–Y alloy (Mg$_{55}$Y, 1.82 at.% Y) are shown in figure 4. In the four GSFE curves, there is only one global maximum corresponding to the unstable stacking fault energy (USFE) of the studied slip system. Based on our DFT calculations, the USFE is 44% lower in the Mg–Y alloy (0.128 J m^{-2}) than in pure Mg (0.231 J m^{-2}). The latter value
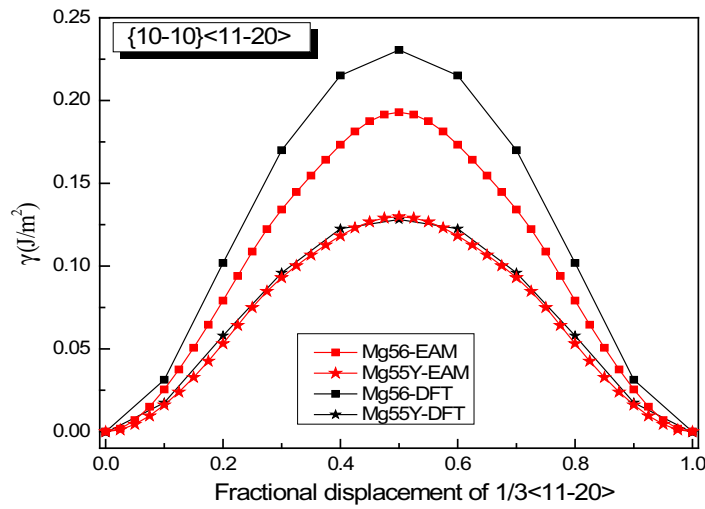
Figure 4. Same as in figure 3 but for the $\langle 11\bar{2}0 \rangle$ direction in the prismatic plane. The total displacement is equal to the corresponding lattice parameter a of either pure Mg or Mg–Y alloy ($Mg_{55}Y$).
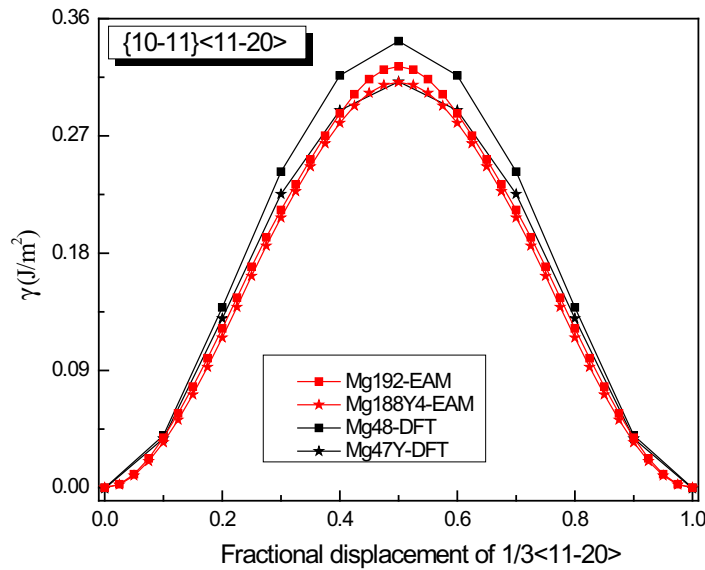

Figure 5. Same as in figures 3 and 4 but along the $\langle 11\bar{2}0 \rangle$ direction in the pyramidal plane.

for elemental Mg is in good agreement with previous DFT studies for pure Mg that reported $0.218\,\mathrm{J\,m^{-2}}$ [16] and $0.225\,\mathrm{J\,m^{-2}}$ [17]. The corresponding EAM results are qualitatively very similar but the predicted reduction is lower. Therefore, despite the fact that the actual energy barriers obtained by DFT and EAM calculations differ, the changes induced by Y alloying are qualitatively very similar and thus independent of our selected computational method.

3.1.3. Pyramidal $\{10\bar{1}1\}\langle 11\bar{2}0 \rangle$ slip system. The GSFE results computed for the $\{10\bar{1}1\}\langle 11\bar{2}0 \rangle$ pyramidal slip system are visualized in figure 5. The GSFE curves of the Mg–Y alloy
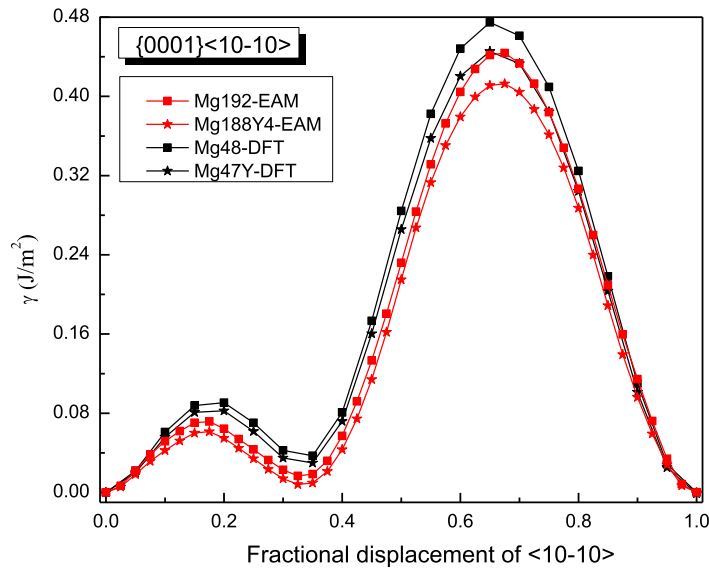
Figure 6. Same as in figures 3–5 but along the $\langle 10\bar{1}0 \rangle$ direction in the basal plane. The total displacement is $\frac{\sqrt{3}}{3}a$, with a being the lattice parameter of either pure Mg or Mg–Y alloy (Mg$_{47}$Y). The stable stacking fault energy and that of the unstable one correspond to displacements $\frac{1}{3}a$ and $\frac{2}{3}a$, respectively.

calculated by DFT and EAM methods match very well. As in the case of the $\{0001\}\langle 11\bar{2}0 \rangle$ and $\{10\bar{1}0\}\langle 11\bar{2}0 \rangle$ slip systems, the GSFEs predicted for pure Mg differ slightly. However, irrespective of the computational method used, GSFE values are lower in Mg–Y than those determined for pure Mg. Hence the DFT-calculated USFEs in Mg–Y alloys are reduced by 9% (from $0.343 \, \text{J m}^{-2}$ calculated for pure Mg). The corresponding EAM values indicate a reduction by 4% (from $0.323 \, \text{J m}^{-2}$ in pure Mg). The DFT-based USFE of pure Mg is in very good agreement with previous DFT results [14, 17].

3.1.4. The $\{0001\}\langle 10\bar{1}0 \rangle$ slip system. The computed GSFE curves for the $\{0001\}\langle 10\bar{1}0 \rangle$ slip system of pure Mg and Mg$_{47}$Y (2.08 at.%) are plotted as a function of the applied shift vector in figure 6. The four curves show similar characteristics, e.g. a local minimum corresponding to the displacement of $\approx \frac{1}{3}$ and a global maximum at a shift of about $\frac{2}{3}$ of the perfect lattice vector. The local minimum corresponds to the local stacking configuration ($\ldots$ABABCACACA$\ldots$), which is the I$_2$ SFE. The I$_2$ SFEs in pure Mg and Mg$_{47}$Y calculated by DFT are 0.037 and $0.030 \, \text{J m}^{-2}$, respectively, and so they exhibit a reduction by $0.007 \, \text{J m}^{-2}$ due to the Y atoms. The EAM values differ slightly but are qualitatively similar, with an I$_2$ SFE of $0.017 \, \text{J m}^{-2}$ (in pure Mg) being reduced by 0.009 to $0.008 \, \text{J m}^{-2}$ (in the Mg$_{47}$Y alloy).

The global maximum of these GSFE curves corresponds to the stacking fault ($\ldots$ABABABBCBCBC$\ldots$), which is characterized by the on-top position of the two atomic planes across the fault plane. The energy of this configuration in Mg and the Mg–Y alloy was found to be 0.475 and $0.445 \, \text{J m}^{-2}$, respectively, using DFT. The EAM calculated energies of these maxima are 0.444 and $0.413 \, \text{J m}^{-2}$, respectively, closely matching the corresponding Y-induced reduction in the USF energy predicted by DFT. Here we can conclude that irrespective of the material system (Mg or Mg–Y alloys), the GSFEs calculated by the EAM are
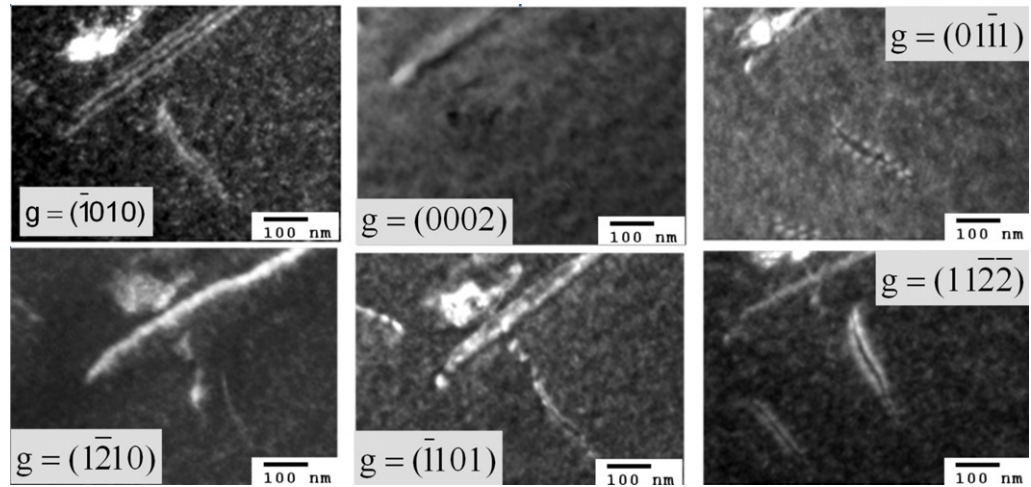
Figure 7. Weak-beam dark field TEM micrographs of an I_2 stacking fault under different two-beam conditions. From the visibility of the bounding partial dislocations under the different diffraction conditions, their Burgers vectors were determined: $b = 1/3\,[\,10\bar{1}0]$ and $b = 1/3\,[\,01\bar{1}0]$.

apparently lower than those obtained using DFT. However, the trend of a Y-induced reduction in the GSFE is the same. The DFT-calculated energies of local GSFE maxima and minima (I_2 SFE) are in quantitative agreement with previous results [13, 16, 17].

In order to verify this theoretical prediction that Y additions lower the I_2 stacking fault, an experimental TEM study has been performed (for details related to TEM measurements, see our previous paper [5]). These TEM observations on slightly pre-deformed (1.5%) pure Mg and Mg–3Y (wt.%) were performed to measure the I_2 SFE. In pure Mg no I_2 stacking faults were observed, which indicates a relatively high stacking fault energy, i.e. a low probability to form these stacking faults or a dissociation width that is too small to be measured using conventional TEM. In Mg–3Y, frequent formation of the I_2 stacking fault was observed allowing the measurement of the I_2 SFE, figure 7. Here, the Burgers vectors (**b**) of the bounding partial dislocations of the stacking faults were determined according to the $\mathbf{g} \cdot \mathbf{b}$ invisibility criterion, figure 7. Both bounding partial dislocations are invisible under $\mathbf{g} = (0002)$, only one is visible under $\mathbf{g} = (1\bar{2}10)$ and both are visible under $\mathbf{g} = (\bar{1}010)$, $(01\bar{1}1)$, $(\bar{1}101)$ and $(11\bar{2}\bar{2})$, figure 7. Therefore, it is concluded that one partial dislocation has the Burgers vector $\mathbf{b} = 1/3\,[10\bar{1}0]$ and the other has the Burgers vector $\mathbf{b} = 1/3\,[01\bar{1}0]$ building an I_2 stacking fault according to the dissociation reaction: $1/3\,[11\bar{2}0] \rightarrow 1/3\,[10\bar{1}0] + 1/3\,[\,01\bar{1}0]$. The corresponding stacking fault energies are calculated based on the dissociation width of the partial dislocations according to equation

$$\gamma = \frac{Gb^2}{8\pi d}\frac{2-v}{1-v}\left(1 - \frac{2v}{2-v}\cos 2\beta\right).$$

Here, γ is the stacking fault energy, G the shear modulus, v the Poisson's ratio, **b** the Burgers vector of the partials, β the angle between the partials and d the splitting width of the partials. Consequently, the I_2 stacking fault energy of Mg–Y amounts to $1.5 \pm 0.5\ \mathrm{mJ\,m^{-2}}$ with an average dissociation width of about 20–30 nm.
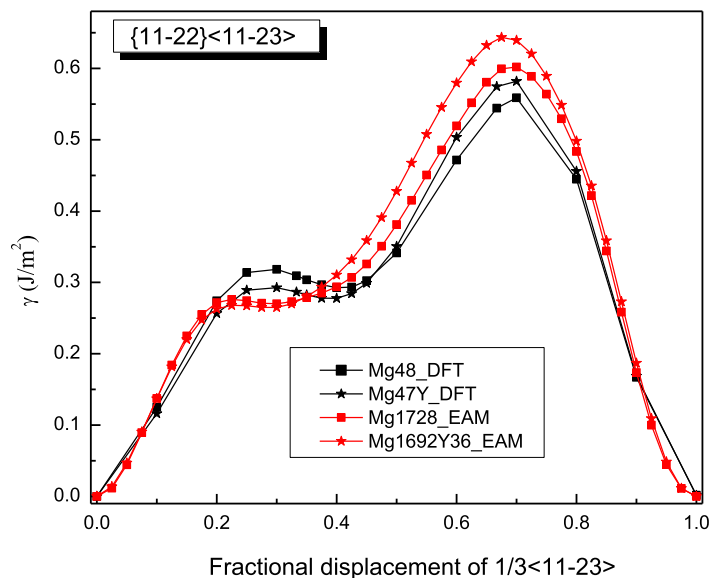
Figure 8. GSFE profiles calculated for the elemental Mg and Mg alloys as a function of the shifted displacement along the $\langle 11\bar{2}3 \rangle$ direction in the non-basal plane $\{11\bar{2}2\}$. The total displacement is the length of the Burgers vector $\frac{1}{3}\langle 11\bar{2}3 \rangle$. The stable stacking fault energies, local unstable ones and global unstable ones correspond to crystal displacements of about 0.4, 0.25 and 0.7 calculated by DFT, and about 0.3, 0.22 and 0.7, respectively, by EAM.

3.2. Non-basal plane generalized stacking fault energies

As the $\{11\bar{2}2\}\langle 11\bar{2}3 \rangle$ slip system is an important non-basal slip system, its GSFE was also studied. The GSFE profiles of the slip system are calculated for pure Mg and $Mg_{47}Y$ (2.08 at.%) using both DFT and EAM calculations (see figure 8). The GSFE curves share similar shapes, with two maxima (one local and one global) and a local minimum along the shift vector. The local minimum corresponds to a stable stacking fault energy. The stable stacking fault energy predicted for $Mg_{47}Y$ by DFT ($0.293\,\mathrm{J\,m^{-2}}$) is lower than that in pure Mg ($0.318\,\mathrm{J\,m^{-2}}$). The EAM results suggest a smaller reduction in the stable SFE of only $0.008\,\mathrm{J\,m^{-2}}$ by the addition of Y. The energy difference corresponding to this reduction in the stable SFE is, however, very small and, in fact, quite close to the error bar of our EAM calculations.

The maximum of the GSFE (USFE) calculated by both DFT and EAM is higher in $Mg_{47}Y$ than in pure Mg. The DFT results are again very close to previous DFT results [14]. Both DFT and EAM data clearly indicate that the computed energies for Mg and Mg–Y crystals reverse their mutual order with increasing displacement (see figure 8). Specifically, the generalized stacking fault energies are first nearly equal for both Mg and $Mg_{47}Y$ for displacements lower than 0.2, then Y additions result in a clear lowering of stacking fault energies up to a displacement when GSFE curves of Mg and $Mg_{47}Y$ systems cross and the energies are beyond this point in the system containing the Y atoms. The displacement corresponding to the crossing point is ≈ 0.48 and 0.37 in the case of DFT and EAM results, respectively.

With regard to the local minima and maxima individual, the corresponding fractional displacements are not exactly equal when calculated by DFT and EAM methods.

Table 7. DFT- and EAM-calculated values of stable stacking fault energies S, unstable stacking fault energies U, and their ratio, for pure Mg and Mg–Y alloys for the five selected slip systems. Unstable stacking fault energy U_1 is the local maximum of the γ-surface, and U_2 is the global maximum.

Supercell	DFT				EAM			
	S	U_1	U_2	S/U_1	S	U_1	U_2	S/U_1
1-Mg	–	0.276, 0.288[a]	–	–	–	0.233	–	–
1-Mg–Y	–	0.214, 0.248[a]	–	–	–	0.190	–	–
2-Mg	0.037, 0.036[a], 0.034[b], 0.039[c]	0.091, 0.092[a], > 0.092[b], 0.101[c]	0.475	0.41, 0.39[a], < 0.37[b], 0.39[c]	0.017, 0.044[b]	0.072, 0.082[b]	0.444	0.24, 0.54[b]
2-Mg–Y	0.030, 0.025[a]	0.083, 0.071[a]	0.445	0.36, 0.35[a]	0.008	0.061	0.413	0.13
3-Mg	–	0.231, 0.473[a], 0.218[b], ∼ 0.225[c]	–	–	–	0.266, 0.170[b]	–	–
3-Mg–Y	–	0.128, 0.558[a]	–	–	–	0.124	–	–
4-Mg	–	0.343, 0.310[d] ∼ 0.340[c]	–	–	–	0.323, 0.226[d]	–	–
4-Mg–Y	–	0.312	–	–	–	0.311	–	–
5-Mg	0.298, 0.236[d]	0.318, 0.243[d]	0.559, 0.485[d]	0.94, 0.97[d]	0.270, 0.198[d]	0.276, 0.206[d]	0.602, 0.505[d]	0.98, 0.96[d]
5-Mg–Y	0.278	0.293	0.582	0.95	0.265	0.268	0.644	0.989

The energies in the table are in $J\,m^{-2}$. The numbers before the names of material systems denote different slip systems. 1—$\{0001\}\langle11\bar{2}0\rangle$, 2—$\{0001\}\langle1\bar{1}00\rangle$, 3—$\{10\bar{1}0\}\langle11\bar{2}0\rangle$, 4—$\{10\bar{1}1\}\langle11\bar{2}0\rangle$, 5—$\{11\bar{2}2\}\langle11\bar{2}3\rangle$. The EAM data from [16] are the results of Sun EAM. The data taken from [17] are the results of KSDFT/LDA/TM-NLPS.
[a] Muzyk *et al* [13].
[b] Yasi *et al* [16].
[c] Shin *et al* [17].
[d] Nogaret *et al* [14].

The DFT-calculated shallow minima ($0.020\,J\,m^{-2}$ for Mg and $0.015\,J\,m^{-2}$ for $Mg_{47}Y$) indicate a dissociation of the perfect $\frac{1}{3}\langle11\bar{2}3\rangle$ dislocation family into partial dislocations according to the following reaction:

$$\frac{1}{3}\langle11\bar{2}3\rangle = \lambda\,\frac{1}{3}\langle11\bar{2}3\rangle + (1-\lambda)\,\frac{1}{3}\langle11\bar{2}3\rangle \ (\lambda \simeq 0.4), \tag{1}$$

where λ is a constant coefficient for the dissociation reaction. For $\lambda = 0.4$, the rows of atoms in the adjacent two gliding planes seem to be more regular than in any other case (see [19], figure 7, $0.6\langle c+a\rangle$).

A dissociation of perfect $\langle c+a\rangle$ dislocations was also found by other authors, but with different λ values. In [14], based on DFT and EAM (Liu potential), values of $\lambda = 0.33$ and 0.25, respectively, were found for pure Mg. In [19], a λ value of 0.5 was reported using an EAM potential taking in-plane relaxations of the atoms into account. The different λ values are due to the different calculation methods and the specific conditions. Lower SFE and USFE values indicate a tendency toward deformation mechanisms including partial dislocations when compared with pure Mg.

Despite a few discrepancies between DFT and EAM results, it can be concluded that, from a qualitative point of view, the EAM gives a rather accurate description of the GSFE in the
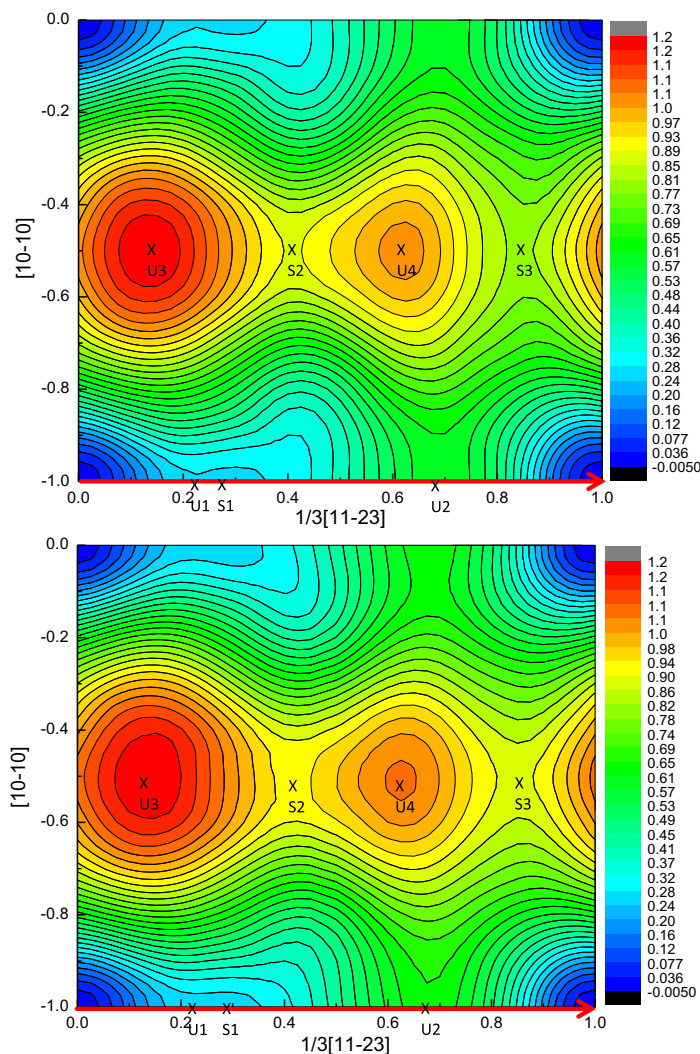
Figure 9. Projection of the $\{11\bar{2}2\}$ plane γ-surface with $0.040\,\text{J}\,\text{m}^{-2}$ isolines for the newly developed EAM potential. The $\frac{1}{3}\langle 11\bar{2}3\rangle$ Burgers vector and the minimum energy path are the same (line in red color). $S1$, $S2$ and $S3$ indicate the three stable stacking faults, and $U1$, $U2$, $U3$ and $U4$ the unstable stacking faults. The generalized stacking fault energies of $U1$, $U2$ and $S1$ are U_1, U_2 and stable stacking faults calculated using EAM potentials in table 7. For $U3$, $U4$, $S2$ and $S3$, the corresponding GSF energies are (a) 1.218, 1.033, 0.889 and $0.807\,\text{J}\,\text{m}^{-2}$ and (b) 1.226, 1.075, 0.930 and $0.888\,\text{J}\,\text{m}^{-2}$.

$\{11\bar{2}2\}\langle 11\bar{2}3\rangle$ glide system. In particular, the trend that alloying Y in Mg reduces stable stacking fault energies is correctly captured. Further details related to the $\{11\bar{2}2\}\langle 11\bar{2}3\rangle$ stable stacking faults will be described in the next subsection.

The calculated results obtained for the five studied slip systems are summarized in table 7 together with published data. The maxima along the GSFE profiles corresponding to the three basal slip systems indicate that the highest unstable stacking fault energy is expected for $\frac{1}{3}\langle 11\bar{2}0\rangle$ dislocations on the pyramidal plane and the lowest on the prismatic plane. The ratios

between the stable and unstable stacking fault energies are calculated for the $\{0001\}\langle10\bar{1}0\rangle$ and $\{11\bar{2}2\}\langle11\bar{2}3\rangle$ slip systems. The actual results are listed in table 7. Moreover, table 7 reveals that the ratio between the stable and unstable stacking fault energies decreases in the $\{0001\}\langle10\bar{1}0\rangle$ slip system upon alloying with Y, further supporting the conclusion that Y alloying lowers the SFE. For the $\{11\bar{2}2\}\langle11\bar{2}3\rangle$ slip system there is a more complex change of the positions and ratio of the stable and unstable stacking fault energies, and so the influence of Y atoms is more complex and a topic for future study.

3.3. Non-basal plane γ-surfaces

In order to deepen our understanding of $\langle11\bar{2}3\rangle$ non-basal slip processes and stable staking faults on the $\{11\bar{2}2\}$ plane, the GSFEs in pure Mg and Mg–Y alloys were calculated employing our newly developed EAM potentials (see figure 9). There is no significant difference between the γ-surfaces for pure Mg and Mg–Y. In both figures 9(a) and (b), the lowest-energy slip path is a line section along $y = 0$, which is exactly the Burgers vector $\frac{1}{3}\langle11\bar{2}3\rangle$.

Another path connects two maxima (marked as $U1$ and $U2$) and one minimum (marked $S1$) without consideration of the point where $x = 0$ and $y = 0$. This can be seen in figure 8. There are also another two minima ($S2$ and $S3$) in the γ surface, but their energies are both much higher than that of $S1$. So the $S1$ minimum is the most stable stacking fault on the $\{11\bar{2}2\}$ plane. The calculation of the γ-surface for pure Mg was performed in [19] (see figure 4 in [19]), and quantitatively agrees with our results. Along $[10\bar{1}0]$, there exists a curved minimum path across the $S3$ point. The fact that the energy at the $S3$ point is even higher than that calculated for $U2$ shows that this minimum path is not energetically favorable.

4. Conclusions

Using DFT and newly developed EAM potentials, we present GSFE profiles for five selected slip systems in both pure Mg and Mg–Y alloys. The results of the three $\langle a\rangle$ slip systems show that the USFEs decrease upon Y additions in Mg. From the slip system $\{0001\}\langle10\bar{1}0\rangle$ the I_2 SFE values for pure Mg and Mg–Y are obtained, and the I_2 SFE of Mg–Y alloy is again lower than that computed for pure Mg. Importantly, the generalized stacking fault energies associated with displacement along the $\langle11\bar{2}3\rangle$ direction in the non-basal plane $\{11\bar{2}2\}$ are initially lower but with increasing displacement become higher than those of Mg. This is in contrast to the basal slip systems, for which the Mg–Y energies are consistently lower than for Mg. Lastly, after careful testing of our newly developed EAM Mg–Y potential, the generalized stacking fault energies for all glide systems within the $\{11\bar{2}2\}$ plane are calculated using this potential and the GSFE profiles are visualized as a two-dimensional γ-surface. Our theoretical study has been complemented by an experimental TEM analysis that confirmed our theoretical prediction that the I_2 stacking fault energy is reduced due to Y additions.

To summarize, as a complement to previous experimental studies, we use theoretical methods to decompose the complex interplay of various mechanisms acting in Mg alloys in order to study some of them individually. Focusing solely on a few selected slip systems, we conclude that the impact of Y additions on generalized stacking fault energies is rather complex. On the one hand, the Y atoms reduce both stable and unstable stacking fault energies in the case of studied $\langle a\rangle$ slip systems. On the other hand, this influence may not be generalized to all slip systems as we predict also an increase of energies due to Y additions for most of the

displacements along the $\langle 11\bar{2}3 \rangle$ direction in the non-basal plane $\{11\bar{2}2\}$ and a shift in position of stable SF. Due to the fact that previous studies of fcc materials linked the stable and unstable stacking fault energies with the mobility and activity of dislocations, we speculate that our findings can have similar consequences in the case of Mg alloys. As a verification of this speculation will necessarily require further theoretical studies addressing the full complexity of these materials, we have also developed and carefully tested a new EAM potential. The comparison of first-principles and EAM results indicates that our EAM potential may be suitable for future larger-scale atomistic simulations.

Acknowledgments

References

[1] Kainer K U 2000 *Magnesium Alloys and their Applications* (Weinheim: Wiley)
[2] Friedrich H E *et al* 2006 *Magnesium Technology* (Berlin: Springer)
[3] Couling S L, Pashak J F and Sturkey L 1969 *Trans. ASM* **51** 94–107
[4] Yoo M H, Morris J R, Ho K M and Agnew S R 2002 Nonbasal deformation modes of HCP metals and alloys: role of dislocation source and mobility *Metall. Trans.* A **33A** 813–22
[5] Sandlöbes S, Zaefferer S, Schestakow I, Yi S and Gonzalez-Martinez R 2011 On the role of non-basal deformation mechanisms for the ductility of Mg and Mg–Y alloys *Acta Mater.* **59** 429–39
[6] Tonda H and Ando S 2002 Effect of temperature and shear direction on yield stress by $\{11(2)-2\}\langle(11)-23\rangle$ slip in HCP metals *Metall. Mater. Trans.* A **33A** 831–6
[7] Koike J, Kobayashi T, Mukai T, Watanabe H, Suzuki M, Maruyama K and Higashi K 2003 The activity of non-basal slip systems and dynamic recovery at room temperature in fine-grained AZ31B magnesium alloys *Acta Mater.* **51** 2055–65
[8] Agnew S R, Horton J A and Yoo M H 2002 Transmission electron microscopy investigation of $\langle c+a \rangle$ dislocations in Mg and alpha-solid solution Mg–Li alloys *Metall. Mater. Trans.* A **33A** 851–8
[9] Thornburg D R and Piehler H R 1975 Analysis of constrained deformation by slip and twinning in hexagonal closed packed metals and alloys *Metall. Trans.* A **6A** 1511–23
[10] Yoo M H 1981 *Metall. Trans.* A **12A** 409–18
[11] Yoo M H and Lee J K 1991 Deformation twinning in hcp metals and alloys *Phil. Mag.* A **63** 987–1000
[12] Vítek V 1968 *Phil. Mag.* **18** 773–86
[13] Muzyk M, Pakiela Z and Kurzydlowski K J 2012 Generalized stacking fault energy in magnesium alloys: density functional theory calculations *Scr. Mater.* **66** 219–22
[14] Nogaret T, Curtin W A, Yasi J A, Hector L G Jr and Trinkle D R 2010 Atomistic study of edge and screw $\langle c+a \rangle$ dislocations in magnesium *Acta Mater.* **58** 4332–43
[15] Han J, Su X M, Jin Z-H and Zhu Y T 2011 Basal-plane stacking-fault energies of Mg: a first-principles study of Li- and Al-alloying effects *Scr. Mater.* **64** 693–6

[16] Yasi J A, Nogaret T, Trinkle D R, Qi Y, Hector L G Jr and Curtin W A 2009 Basal and prism dislocation cores in magnesium: comparison of first-principles and embedded-atom-potential methods predictions *Modelling Simul. Mater. Sci. Eng.* **17** 055012

[17] Shin I and Carter E A 2012 Orbital-free density functional theory simulations of dislocations in magnesium *Modelling Simul. Mater. Sci. Eng.* **20** 015006

[18] Tadmor E B and Bernstein N 2004 A first-principles measure for the twinnability of FCC metals *J. Mech. Phys. Solids* **52** 2507

[19] Morris J R, Scharff J, Ho K M, Turner D E, Ye Y Y and Yoo M H 1997 Prediction of a {11(2)-2} hcp stacking fault using a modified generalized stacking-fault calculation *Phil. Mag.* **76** 1065–77

[20] Hohenberg P and Kohn W 1964 Inhomogeneous electron gas *Phys. Rev.* **136** B864

[21] Kohn W and Sham L J 1965 Self-consistent equations including exchange and correlation effects *Phys. Rev.* **140** A1133

[22] Daw M S and Baskes M I 1984 Embedded-atom method—derivation and application to impurities, surfaces and other defects in metals *Phys. Rev.* B **29** 6443

[23] Plimpton S 1995 Fast parallel algorithms for short-range molecular-dynamics *J. Comput. Phys.* **117** 1

[24] Foiles S M, Baskes M I and Daw M S 1986 Embedded-atom-method functions for the fcc metals Cu, Ag, Au, Ni, Pd, Pt and their alloys *Phys. Rev.* B **33** 7983

[25] Sheng H W, Kramer M J, Cadien A, Fujita T and Chen M W 2011 Highly-optimized EAM potentials for 14 fcc metals *Phys. Rev.* B **83** 134118

[26] Ercolessi F and Adams J B 1994 Interatomic potentials from 1st-principles calculations—the force-matching method *Europhys. Lett.* **26** 583

[27] Brommer P and Gahler F 2007 Potfit: effective potentials from *ab initio* data *Modelling Simul. Mater. Sci. Eng.* **15** 295

[28] Villars P 1997 *Pearson's Handbook* desk edn (Materials Park, OH: ASM International)

[29] Kresse G and Hafner J 1994 *Ab-initio* molecular-dynamics simulation of the liquid-metal amorphous-semiconductor transition in germanium *Phys. Rev.* B **49** 14251

[30] Sun D Y, Mendelev M I, Becker C A, Kudin K, Haxhimali T, Asta M, Hoyt J J, Karma A and Srolovitz D J 2007 Crystal-melt interfacial energies in hcp metals: a molecular dynamics study of Mg *Phys. Rev.* B **73** 024116

[31] Liu X Y, Adams J B, Ercolessi F and Moriarty J A 1996 EAM potential for magnesium from quatum mechanical forces *Modelling Simul. Mater. Sci. Eng.* **4** 293

[32] Hu W Y B., Zhang W, Huang B Y, Gao F and Bacon D J 2001 Analytic modified embedded atom potentials for HCP metals *J. Phys.: Condens. Matter* **13** 1193

[33] Baskes M I and Johnson R A 1994 Modified embedded-atom potentials for hcp metals *Modelling Simul. Mater. Sci. Eng.* **2** 147

[34] Barrett C S and Massalski T B 1966 *Structure of Metals* (New York: McGraw-Hill)

[35] Kittel C 1976 *Introduction to Solid State Physics* (New York: Wiley)

[36] Simons G and Wang H 1977 *Single Crystal Elastic Constants and Calculated Aggregate Properties* (Cambridge, MA: MIT Press)

[37] de Boer F R, Boom R, Matterns W C M, Miedema A R and Niessen A K 1988 *Cohesion in Metals; Transition Metal Alloys* (Amsterdam: North-Holland)

[38] Campbell F C 2008 *Elements of Metallurgy and Engineering Alloys* (Materials Park, OH: ASM International)

[39] Blöchl P E 1994 Projector augmented-wave method *Phys. Rev.* B **50** 17953

[40] Perdew J P, Burke K and Ernzerhof M 1996 Generalized gradient approximation made simple *Phys. Rev. Lett.* **77** 3865

[41] Kresse G and Furthmüller J 1996 Efficient iterative schemes for *ab initio* total-energy calculations using a plane-wave basis set *Phys. Rev.* B **54** 11169

[42] Kresse G and Joubert J 1999 From ultrasoft pseudopotentials to the projector augmented-wave method *Phys. Rev.* B **59** 1758

[43] Monkhorst H J and Pack J D 1976 Special points for Brillouin-zone integrations *Phys. Rev.* B **13** 5188

[44] Lide D R 2005–2006 *Handbook of Chemistry and Physics* 86th edn (Boca Raton, FL: CRC Press)

[45] Hu W, Xu H, Shu X, Yuan X, Gao B and Zhang B 2000 Calculation of thermodynamic properties of Mg–RE (RE = Sc, Y, Pr, Nd, Gd, Tb, Dy, Ho or Er) alloys by an analytic modified embedded atom method *J. Phys. D: Appl. Phys.* **33** 711

[46] Sandlöbes S, Friák M, Zaefferer S, Dick A, Yi S, Letzig D, Pei Z, Zhu L-F, Neugebauer J and Raabe D 2012 The relation between ductility and stacking fault energies in Mg and Mg–Y alloys *Acta Mater.* **60** 3011–21